Exploring the Activation of Atomically Precise $[Pt_{17}(CO)_{12}(PPh_3)_8]^{2+}$ Clusters: Mechanism and Energetics in Gas Phase and on an Inert Surface

Papri Chakraborty,[#] Marco Neumaier,[#] Johannes Seibel, Nicola Da Roit, Artur Böttcher, Christian Schmitt, Di Wang, Christian Kübel, Silke Behrens, and Manfred M. Kappes*

ABSTRACT: Atomically precise clusters such as $[Pt_{17}(CO)_{12}(PPh_3)_8]^{x+}$ (x = 1,2) (PPh_3 is triphenylphosphine) are known as precursors for making oxidation catalysts. However, the changes occurring to the cluster upon thermal activation during the formation of the active catalyst are poorly understood. We have used a combination of hybrid mass spectrometry and surface science to map the thermal decomposition of $[Pt_{17}(CO)_{12}(PPh_3)_8]$ $(NO_3)_2$. High-resolution mass and ion mobility spectrometry together with DFT-based modeling were used to probe the sequence of fragmentation reactions and fragment structures generated upon collisional excitation of $[Pt_{17}(CO)_{12}(PPh_3)_8]^{2+}$. This was compared with thermal desorption spectroscopy of $[Pt_{17}(CO)_{12}(PPh_3)_8]$ $(NO_3)_2$ dropcast onto an inert graphite surface. In both cases, a characteristic sequence of CO and benzene desorption steps is observed followed at higher excitation energy by H_2 loss. This behavior is indicative of Pt-catalyzed C−H activation of phenyl groups during partial stripping of the ligand shell while the $Pt_{17}P_8$ cluster core is retained.

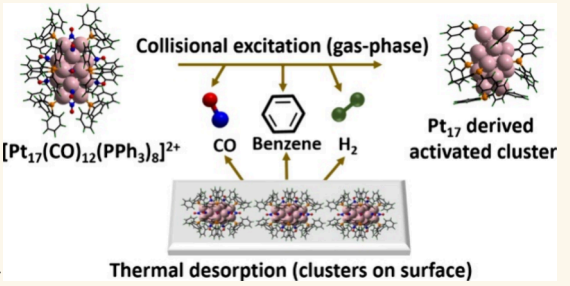

KEYWORDS: *platinum clusters, nanocatalysis, mass spectrometry, ion mobility, thermal desorption spectroscopy*

1. INTRODUCTION

Industrial catalysts based on noble metal nanoparticles (NP) supported on metal oxides have significant societal impact, e.g. in control of pollutants emitted upon combustion of hydrocarbons.[1] T hese catalyst systems have typically been optimized to function over long time scales at elevated temperatures−oftentimes also subject to periodically repeated regeneration procedures when their activity begins to degrade.[2] Much if not all of the associated preparation, activation, operation and regeneration is based more on empiricism at the mesoscale rather than on detailed mechanistic insight at an atomic level. While this approach has worked out well in the past−in the case of automotive emission catalysis for over 50 years−recent global developments require improved catalyst efficiencies an d si gnificant red uction in the amo unt of raw materials and/or energy consumption required to make and run the catalysts.

A promising approach in this regard is to generate a catalyst by thermal activation of preformed, atomically precise, ligand stabilized metal clusters.[3−8] Such rigorously monodispersed species typically comprising less than 100 metal atoms optimize the number of their surface versus bulk atoms thus potentially saving on overall metal loading−given sufficient turnover frequencies per exposed catalytically active metal atom. Negishi et al. have recently described a simple synthesis procedure for a new cluster $[Pt_{17}(CO)_{12}(PPh_3)_8]^{x+}$, x = 1 and 2 (with Cl^- and SbF_6^- counterions)[9] which when deposited onto γ -alumina can be calcined to generate a highly active "Pt_{17}" based CO oxidation catalyst.[10] In fact, when coated onto a cordierite honeycomb substrate (as used in automotive catalysis), "Pt_{17}" is reported to have an activity which is better than that of a standard Pt NP catalyst prepared by the impregnation method on the same support - even after aging

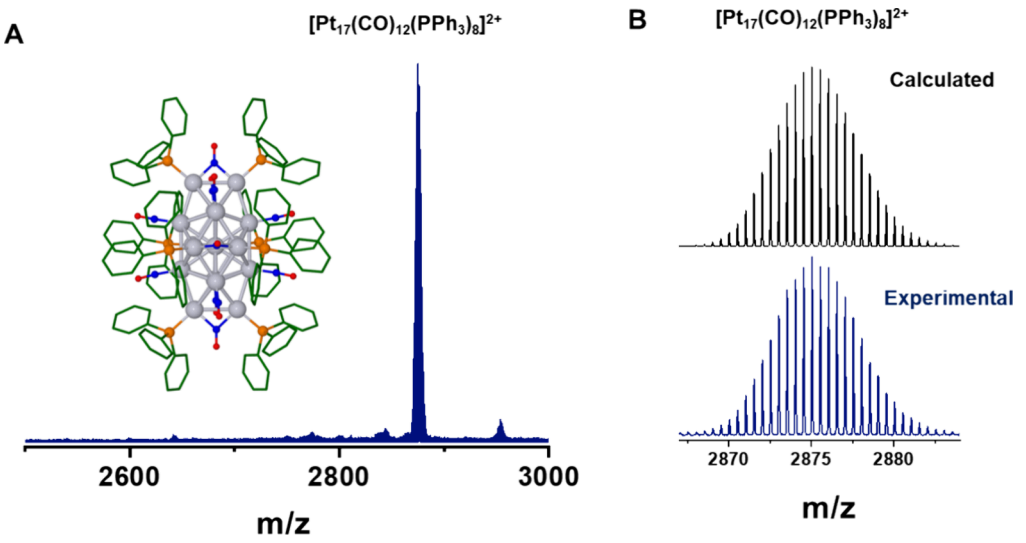

Figure 1. (A) Typical positive ion ESI mass spectrum obtained for a solution of $[Pt_{17}(CO)_{12}(PPh_3)_8](NO_3)_x$ (x = 1,2), together with a schematic molecular structure of the primary ion $[Pt_{17}(CO)_{12}(PPh_3)_8]^{2+}$ (gray: Pt atoms, orange: P atoms, blue and red: C and O of CO, green: C of C_6H_5 moieties of PPh_3, H atoms not shown for clarity). (B) Comparison of experimental and calculated isotopologue distribution of $[Pt_{17}(CO)_{12}(PPh_3)_8]^{2+}$.

under operating conditions.[10] This was established in a near atmospheric pressure flow reactor study using a gas mixture consisting of 1% CO, 0.5% O_2, and 98.5% N_2 which was circulated over the $[Pt_{17}(CO)_{12}(PPh_3)_8]^{x+}$ (x = 1, 2) coated substrate (0.15 wt % Pt) at a space velocity of 50,000 L h^{-1} while ramping up the temperature to 400 °C at a rate of 20 °C min^{-1}.[10] The authors also presented HAADF-STEM images of the deposited cluster sample after calcination to 500 °C. Interestingly, the STEM images after calcination showed a narrow size distribution of Pt containing particles (1.07 ± 0.24 nm) with sizes similar to that of the initially deposited $[Pt_{17}(CO)_{12}(PPh_3)_8]^{x+}$ on γ- Al_2O_3 (0.94 ± 0.16 nm).[10] Furthermore, a comparison of the individually resolved particles before and after calcination showed that the size and ellipsoidal shape of their central noble metal cluster core does not significantly change.

In other words, "Pt_{17}" (supported on γ- Al_2O_3) appears quite robust to thermal sintering and other degradation processes associated with exposure to O_2 at elevated temperatures. Additionally, it is an active CO oxidation catalyst which can be easily generated from a well-defined $[Pt_{17}(CO)_{12}(PPh_3)_8]^{x+}$ molecular precursor. This makes it a promising "Pt-efficient" catalyst system for understanding reaction mechanisms and further optimizing both active sites and interactions with supports - with atomic precision.

We have recently also become interested in this system and have contributed to a continuous flow, scaled-up synthesis procedure for $[Pt_{17}(CO)_{12}(PPh_3)_8](NO_3)_x$ (x = 1,2).[11] A first step toward uncovering the "Pt_{17}" active site(s) is to study just the thermal decomposition of the $[Pt_{17}(CO)_{12}(PPh_3)_8]^{x+}$ precursor itself under simplified conditions of little or no support interaction in vacuum. The observed dissociation reactions and structural information concerning the major fragments can provide some of the information necessary to understand and model calcination and reactivity of species ensuing upon activation when deposited on a "real world" metal oxide support.

In this study, we present and compare results for: (i) collision induced dissociation of $[Pt_{17}(CO)_{12}(PPh_3)_8]^{2+}$ cluster cations in inert N_2 collision gas - specifically probing the mass, composition and ion mobilities of the fragment ions (and corresponding neutrals) generated - and (ii) thermal decomposition and desorption of neutral species from $[Pt_{17}(CO)_{12}(PPh_3)_8](NO_3)_2$ drop cast onto an inert HOPG substrate and heated under vacuum. Interestingly, we observe the same sequence of fragmentation steps in both experiments. Together with quantum chemical calculations this allows insight into fragment structures and energetics relevant to the transformation of $[Pt_{17}(CO)_{12}(PPh_3)_8](NO_3)_2$ into an active catalyst for CO oxidation.

2. EXPERIMENTAL RESULTS

2.1. Characterization of the Atomically Precise Cluster. A typical ESI mass spectrum of the purified $[Pt_{17}(CO)_{12}(PPh_3)_8](NO_3)_2$ cluster dissolved in 1:1 methanol/toluene is presented in Figure 1A. This shows a peak at m/z 2875 corresponding to the molecular ion $[Pt_{17}(CO)_{12}(PPh_3)_8]^{2+}$ (isotopologue distribution in Figure 1B). The cluster predominantly sprays as a dication under our experimental conditions. A smaller fraction of ~10% was present as a monocation $[Pt_{17}(CO)_{12}(PPh_3)_8]^{+}$ at m/z 5750 (Figure S1). The DFT-optimized structure of the dication cluster (based on the coordinates from the $[Pt_{17}(CO)_{12}(PPh_3)_8][(SbF_6)_2]$ crystal structure[9]) is presented in the inset of Figure 1A. The overall ellipsoidal structure of $[Pt_{17}(CO)_{12}(PPh_3)_8]^{2+}$ constituting a Pt_{13} icosahedral core, is further capped by four Pt atoms. These capping Pt atoms are present as two $Pt_2(\mu_2\text{-}CO)(PPh_3)_2$ units above and below the icosahedral core, respectively. Apart from the two terminal μ2-CO associated with the caps, two more μ2-CO are present in the equatorial region. The cluster is further symmetrically covered by 8 μ_1-CO and 4 PPh_3 ligands. We also synthesized the cluster using perdeuterated PPh_3 and the formation of the isotopically labeled cluster, $[Pt_{17}(CO)_{12}(PPh_3\text{-}d15)_8](NO_3)_2$ was confirmed by ESI MS which showed the molecular ion peak at m/z 2935, corresponding to $[Pt_{17}(CO)_{12}(PPh_3\text{-}d15)_8]^{2+}$ (Figure S2).

2.2. Gas-Phase Measurements. $[Pt_{17}(CO)_{12}(PPh_3)_8]^{2+}$ cations were transferred into the gas-phase by electrospray ionization and subjected to collision induced fragmentation. The resulting fragment structures were characterized by ion mobility spectrometry. This was done using a Waters Select Series Cyclic Ion Mobility Mass Spectrometer (Cyclic IMS-MS).[12,13] ESI conditions were chosen such that transfer of cations from solution occurred essentially

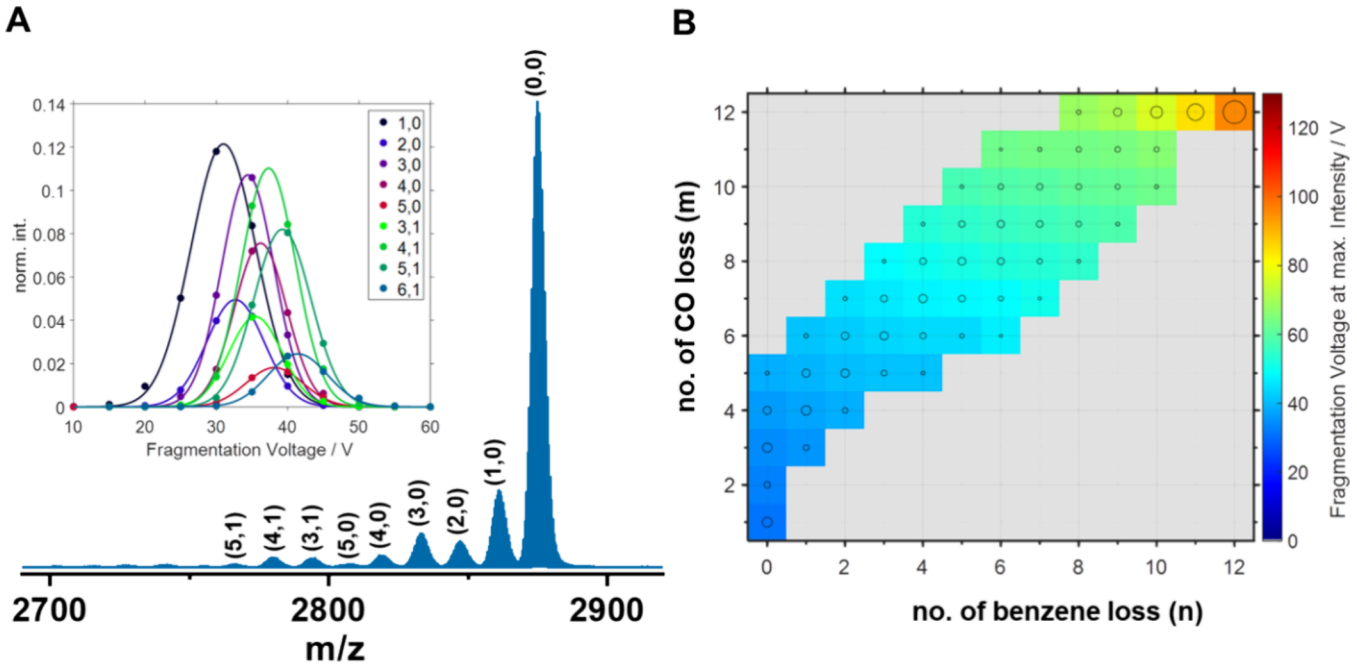

Figure 2. (A) CID mass spectrum of $[Pt_{17}(CO)_{12}(PPh_3)_8]^{2+}$ at a nominal collision voltage of 30 V. Clusters dominantly fragment by losing *m* CO and *n* benzene molecules to form dicationic fragments labeled as (*m*,*n*). The inset shows the collision-voltage resolved intensities of (1−5,0) and (3−6,1). The solid lines show Gaussian fits to the experimental data points. (B) 2D plot of fragmentation voltages at which each (*m*,*n*) fragment dication signal maximizes. The circle size is proportional to normalized ion intensity of each species. Note that at low collision voltages, some CO evolves first before benzene elimination also sets in.

without fragmentation. In similar cases of comparatively large ligand-stabilized metal clusters, we and others have shown that the structures of "parent" ions transferred to gas phase are very similar to those of the corresponding ion in solution or crystal.[13−16] Note that $[Pt_{17}(CO)_{12}(PPh_3)_8]^{2+}$ was the predominant cation obtained by ESI (Figure S1) and we focus on it below.

2.2.1. Collision Induced Dissociation (CID) and Fragment Mass Spectra. 2.2.1.1. Fragmentation Channels and Regimes. To probe CID in N_2, electrosprayed $[Pt_{17}(CO)_{12}(PPh_3)_8]^{2+}$ ions were *m*/*z*-selected in a quadrupole mass filter and transferred into the collision region (trap) of the Cyclic IMS-MS instrument (details of the instrument are described in previous reports[12,13]). Fragment mass spectra were recorded as a function of fragmentation voltages which were systematically varied from 0 to 120 V (Figure 2, Figures S3−S8).

Fragmentation after collisional excitation occurred primarily by sequential loss of small neutral molecules (while the 2+ charge is retained in the larger Pt-containing fragment). Overall, three different fragmentation regimes can be distinguished. At very low collision energies near the fragmentation threshold primarily CO loss is observed (Figure 2A). This is followed at intermediate collision energies by concurrent loss of both CO and benzene moieties (Figure 2B). At highest collisional energies we additionally observe some H, H_2 and C_6H_5 evolution in parallel to CO and benzene (Figure 3). Importantly, over the full collision energy range there is no measurable loss of neutral or small cationic Pt containing moieties and also no charge loss fragmentation pathways leading to the formation of monocationic species (see Figure S3). Furthermore, and in contrast to the case of other PPh_3 protected noble metal clusters in the literature[17,18] we saw no significant desorption of PPh_3 ligands or of any other P containing neutral or cationic moieties (as also checked by comparing to CID of the fully deuterated analogue $[Pt_{17}(CO)_{12}(PPh_3\text{-d15})_8]^{2+}$ (see discussion in SI and Figures S9−S11). We conclude, that collisional excitation leads to partial stripping of the ligand shell while a central dicationic unit comprising all 17 Pt and 8 P atoms is retained. Next, we describe these results in more detail.

2.2.1.2. Collision Energy Dependencies. A CID spectrum at 30 V is presented in Figure 2A. Assignment of the product ions by analysis

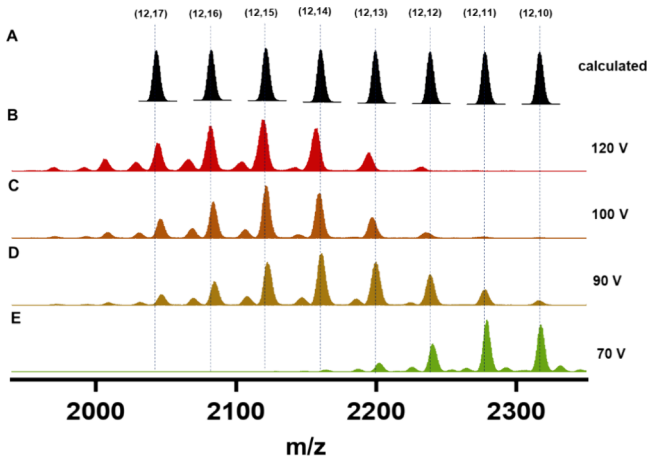

Figure 3. CID mass spectra of $[Pt_{17}(CO)_{12}(PPh_3)_8]^{2+}$ at collision voltages from 70 to 120 V (high collision energy regime). Shown in (A) are the calculated isotopologue distributions for (12,10−17) species (i.e., corresponding to concurrent loss of only CO and benzene). The dotted vertical lines indicate their respective maxima. These are compared in (B−E) to the fragment mass spectra at the collision voltages as indicated. Note slight shifts of fragment mass spectra relative to the dotted lines which indicate additional minor fragmentation channels (as discussed in the text and shown in more detail in the SI).

of their *m*/*z* values and isotopic patterns shows loss of CO and benzene. The peaks are labeled as (*m*,*n*), where *m* and *n* denotes the number of lost CO and benzene molecules, respectively. The peak (0,0) corresponds to the precursor ion $[Pt_{17}(CO)_{12}(PPh_3)_8]^{2+}$ at *m*/*z* 2875. At 30 V, fragment ions corresponding to species (1−5,0) and (3−5,1) were observed (Figure 2A).

Fragment mass spectra obtained by further increasing the collision voltage up to 120 V (Figure S3−S8) can be best fit by still assuming that only CO and benzene loss continue to be the dominant

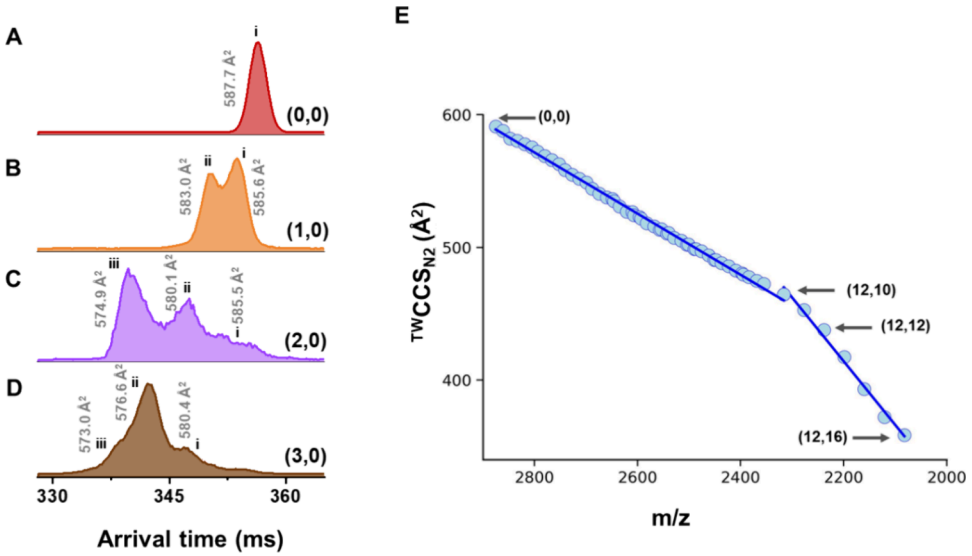

Figure 4. Arrival time distributions recorded after 10 separation passes using cyclic ion mobility spectrometry (cIMS): (A) (0,0), (B) (1,0), (C) (2,0), and (D) (3,0) ions. The $^{TW}CCS_{N2}$ values of the isomers of these species are indicated. These are mean values based on three different measurements. The standard error of the mean is within ±0.3 Å². E) Plot of experimental $^{TW}CCS_{N2}$ values (blue dots; lines are meant to guide the eye) obtained from (lower resolution) single pass measurements for the full range of (*m*,*n*) fragment ions as a function of their *m*/*z* values. Error bars are not shown here for clarity of presentation (see the SI for details).

dissociation channels. Data fitting and peak assignment procedures are discussed in the Supporting Information and shown in Figure S12. This fitting allows to construct a 2D plot of the fragmentation voltages (Figure 2B) at which each fragment species (*m*,*n*) maximizes in terms of ion signal. The respective fragmentation voltages, corresponding to maximum abundance of the (*m*,*n*) species, were obtained from Gaussian fits as shown in the inset of Figure 2A for species (1−5, 0) and (3−6, 1). Fragmentation voltage resolved curves of the other (*m*,*n*) product ions are presented in Figures S13. For instance (1,0) maximizes at 31 V (Figure 2A) which corresponds to the blue data point at *m* = 1 and *n* = 0 in Figure 2B. The size of the circles in Figure 2B is proportional to the normalized ion intensity of each species. Here, the ion intensities of each fragmentation spectrum were normalized to the intensity of the sum of all ions including the (0,0) parent ion, (parent ion is not shown in Figure 2B). For example, at 30 V fragmentation voltage (Figure 2A) the most intense fragment is (1,0) with contribution of ∼12% to the total ion intensity and ∼70% comes from the intact parent ion, i.e. (0,0). Note that Figure 2B only shows fragments down to (12,12), i.e. corresponding to 12 CO and 12 benzene losses. The observation that increasing fragmentation degree requires higher collision energy implies primarily sequential rather than concerted loss.

2.2.1.3. Loss of Benzene via Autocatalytic C−H Activation? Figure 2B shows that up to 5 CO can initially be lost from the precursor ion without any benzene loss occurring. By contrast, the products showing 1 benzene loss are associated with at least 3 (no (1,1) and only traces of (2,1) are seen) and up to 6 CO losses. Together this indicates that a few undercoordinated Pt sites have to be generated before any significant benzene loss can occur. We speculate that these "free Pt atoms" enable *autocatalytic C−H activation of phenyl groups* associated with Pt−C bond formation, H atom transfer to another proximal P−C_6H_5 moiety (or perhaps C_6H_5 transfer to proximal Pt−H to form benzene coordinated with Pt) and then elimination of benzene. As a corollary, for a given cluster to continue to evolve benzene in this way more free Pt atom ensembles have to be generated by further CO loss (the generated sites are progressively "*poisoned*" by Pt−C bond formation). This also explains why all 12 CO's can be stripped off at higher collision energies but no product ions (6−12, 0) are observed.

2.2.1.4. Molecular Hydrogen Evolution via Autocatalytic Dehydrogenation? For higher collision energies fragmentation channels other than CO and benzene begin to also become relevant as indicated by shifts and broadening of the isotopologue distributions corresponding to fragment maxima (12,*n*) with $n \geq 10$. Figure 3 documents small but resolvable shifts in the *m*/*z* values of the isotopologue distributions relative to the theoretical (12,10−17) *m*/*z* values: (i) shifts to higher *m*/*z* can be traced back to additional H atoms that arise from loss of phenyl (−C_6H_5) radicals (or possibly biphenyl molecules) rather than benzene and (ii) shifts to lower *m*/*z* correspond to loss of H (presumably as H_2) from the remaining phenyl rings associated with the P atoms attached to the nanocluster core. Such dehydrogenation was predominantly observed in case of species (12, 12−15). Expanded views of the respective peaks of (12, 12−17) at varying fragmentation voltages of 70−120 V are presented in the Supporting Information (Figure S14−15). This shows loss of up to 12 H (presumably as 6 H_2) from (12,12) and 4 H (presumably as 2 H_2) from (12,15) species. The dehydrogenation behavior was also confirmed by measurements on the deuterated analogue of the cluster i.e., $[Pt_{17}(CO)_{12}(PPh_3\text{-}d15)_8]^{2+}$ (Figure S11). Thermally activated catalytic dehydrogenation of benzene associated with (multiple) Pt−C formation is a known process on Pt single crystal surfaces.[19,20] It is plausible that an analogous process occurs on isolated Pt_{17} nanoclusters.

2.2.2. Characterization of Fragments by Ion Mobility Spectrometry (IMS). IMS has been extensively used to study collision cross sections (CCS) of ligand stabilized coinage metal cluster ions and their fragments in gas-phase.[13,14,21,22] Recently, IMS is also gaining importance in exploring structures of other inorganic molecules.[23−25] Generally, experimental CCS values in molecular nitrogen are compared to DFT derived structural models whose theoretical collision cross sections are determined by trajectory method (TM) simulations for structure assignment. This is the approach we have followed below.

2.2.2.1. $^{TW}CCS_{N2}$ of Fragments Formed at Low Collision Energies. The first steps of the gas-phase dissociation involve the desorption of CO. $[Pt_{17}(CO)_{12}(PPh_3)_8]^{2+}$ (Figure 1A) comprises both on- top and bridging CO ligands, μ_1 and μ_2-CO, respectively. Desorption of CO can occur from several symmetrically nonequivalent sites of both types - in principle giving rise to multiple resolvable isomeric fragments (assuming that specific "CO vacancy" isomers are not interconverting by surface diffusion of ligands on a time scale faster than that of the CCS determination by IMS). To examine this, we performed traveling wave (TW) cyclic IMS (cIMS) studies on the precursor (0,0) and the respective (*m*,0) fragments, for *m* = 1−3,

generated at 35 V. As described in more detail in the methods section the instrument comprises a *cyclic* ion mobility drift cell.[12] Higher ion mobility resolutions can be achieved by increasing the number of passes (cycles) through the cIMS at the expense of reduced ion signal. For this system, 10 passes proved to be an optimum of these counteracting effects.

The species (0−3,0) were each subjected to 10 pass measurements in cIMS. Their respective mobilograms are presented in Figure 4A-D. While the precursor (0,0) showed only one peak (Figure 4A), the fragment ions formed by CO desorption, i.e, (1,0), (2,0) and (3,0) showed multiple peaks corresponding to multiple isomers. The experimental CCS ($^{TW}CCS_{N2}$) of the ions were calculated from their recorded drift times (see details in method section) and their mean values (and standard error of the mean) were calculated based on three measurements on different days (see Figure S16). The species (0,0) showed $^{TW}CCS_{N2}$ of 587.7 ± 0.3 Å^2. For (1,0), two isomers with $^{TW}CCS_{N2}$ of 585.6 ± 0.3 Å^2 and 583.0 ± 0.2 Å^2 are partially resolved (Figure 4B). For (2,0), a larger number of isomers, respectively groups of isomers, can be discerned with $^{TW}CCS_{N2}$ of 585.5 ± 0.2, 580.1 ± 0.2, and 574.9 ± 0.3 Å^2 (Figure 4C). For (2,0), the feature around 585.5 ± 0.2 Å^2 is broader than the other peaks suggesting the presence of additional isomers within the envelope. Similarly, for (3,0), isomer groups with $^{TW}CCS_{N2}$ of 580.4 ± 0.3, 576.6 ± 0.2 and 573.0 ± 0.3 Å^2 were observed (Figure 4D). Note that, the relative differences in $^{TW}CCS_{N2}$ between the successive isomer groups of a particular species are within 1% and cannot be resolved in a single pass measurement (Figure S17). Therefore, multipass measurements were required which show clearly that the initial stages of CO desorption during the activation of $[Pt_{17}(CO)_{12}(PPh_3)_8]^{2+}$ involves multiple isomers at each step.

2.2.2.2. $^{TW}CCS_{N2}$ of Fragments Formed at Intermediate and High Collision Energies. We also determined $^{TW}CCS_{N2}$ for the complete series of (*m*,*n*) fragments (formed over the full collision voltage range studied). To limit measurement time this was done in lower resolution single pass mode rather than by multipass measurements. For the parent ion, i.e. (0,0), for single pass measurement, $^{TW}CCS_{N2}$ is 590.0 ± 0.5 Å^2. Note that the value slightly differs compared to that determined from the 10 passes measurement as discussed above (587.7 ± 0.3 Å^2) as the relative time the ions spend outside the cycle is much larger in a single pass measurement and the calibrant and analyte ions do not necessarily spend the same time outside the cycle. This effect becomes negligible with increasing number of cycles. The resulting single pass $^{TW}CCS_{N2}$ values for the fragment ions (measured on the same day) are listed in Table S1 and plotted as a function of their *m*/*z* values in Figure 4E. This shows a linear decrease of $^{TW}CCS_{N2}$ with *m*/*z* until (12,10) as associated with desorption of CO and benzene. Beyond this, $^{TW}CCS_{N2}$ of the fragments continues to decrease linearly *but with a steeper slope*. As already loss of phenyl ($-C_6H_5$) groups and dehydrogenation start to compete with further benzene loss from (12,10)/(12,11)/(12,12) onward thus complicating the analysis. For determining $^{TW}CCS_{N2}$ of (12,10−16) species, mobilograms were therefore selectively extracted from the *m*/*z* distributions only for (deconvoluted) isotopologue distributions corresponding to benzene loss. Contributions of dehydrogenation or phenyl loss channels were correspondingly excluded. The relative trend in changes in $^{TW}CCS_{N2}$ for the full cascade of (*m*,*n*) fragment ions as a function of their *m*/*z* values was similar when measured on different days, as shown in Figure S18.

2.3. Thermal Desorption Spectroscopy (TDS). For TDS, as-prepared samples of $[Pt_{17}(CO)_{12}(PPh_3)_8](NO_3)_2$ clusters (~0.5 mg) supported on HOPG (~1 cm^2) were inserted into a dedicated UHV apparatus (Depo-0) evacuated to a background pressure below 10^{-8} mbar and heated with a rate of 1.0−1.2 K s^{-1} − see also methods section. Upon heating, desorption of CO, benzene (C_6H_6) and at higher temperatures H_2 was observed in TDS (Figure 5A). Subsequent cooling and reheating the sample lead to no measurable further desorption indicating that complete desorption occurred in the first heating cycle of the TDS experiment. The desorbed products were identified by a quadrupole mass spectrometer with an electron-impact ionization source. H_2^+ (*m*/*z* 2), CO^+ (*m*/*z* 28) and $C_6H_6^+$ (*m*/*z* 78) were the major species detected. Desorption of P containing species was negligible as checked on PH^+ (*m*/*z* 32), PH_2^+ (*m*/*z* 33), PH_3^+ (*m*/*z* 34) and PPh_3^+ (*m*/*z* 226) mass channels (Figure S19). Moreover, no NO_2 desorption from the counterions, as measured on the NO_2^+ mass (*m*/*z* 46) was observed (Figure S19). To clearly distinguish from background signals, desorption of benzene and H_2 was confirmed by performing TDS *on the isotopically substituted perdeuterated cluster*, $[Pt_{17}(CO)_{12}(PPh_3\text{-}d15)_8](NO_3)_2$, which showed desorption of C_6D_6 (detected as $C_6D_6^+$, *m*/*z* 84) (Figure 5Ab) and D_2 (detected as D_2^+, *m*/*z* 4) (Figure 5Ac), respectively. The threshold desorption temperature for CO was ~315 ± 20 K (based on linearized rising flank of the CO desorption signal; Figure 5Aa), which was only marginally lower than that of benzene (~330 ± 20 K; Figure 5Ab). Correspondingly, the desorption of CO and benzene occurred almost simultaneously, reaching maxima at around 400−450 K. The desorption of H_2/D_2 was observed predominantly at significantly higher temperatures, with maxima at around 580−620 K (Figure 5Ac), which is above the temperature required for complete desorption of CO and benzene from the dropcast clusters (at the heating rate and coverages used). For reference, clean HOPG was exposed to air after vacuum annealing and then reinserted for TDS: no measurable desorption was observed in any of the mass channels of interest (Figure S20A). An analogous - negative - reference measurement was performed with just dropcast solvent (Figure S20B).

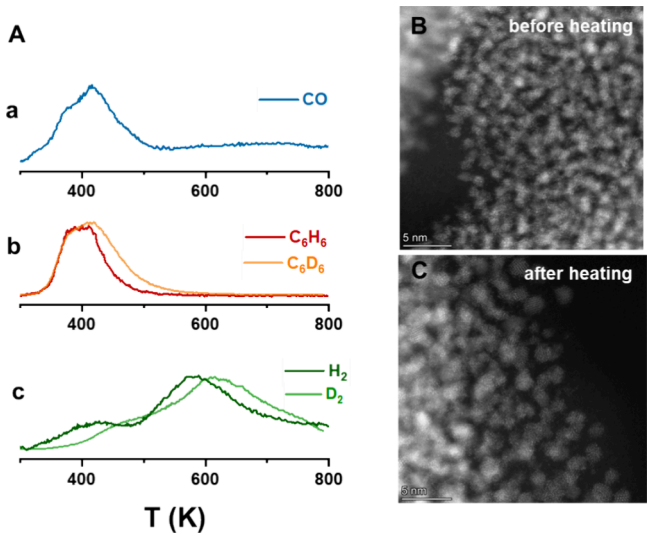

Figure 5. (A) Thermal desorption spectra (*m*/*z*-resolved) recorded in the *m*/*z* channels indicated for solid $[Pt_{17}(CO)_{12}(PPh_3)_8](NO_3)_2$ (respectively the deuterated analogue) dropcast onto ca. 1 cm^2 of freshly cleaved and vacuum annealed HOPG. (B) STEM images of $[Pt_{17}(CO)_{12}(PPh_3)_8](NO_3)_2$ clusters dropcasted on freshly cleaved HOPG. (C) STEM images of the particles recovered after the TDS experiments, i.e., after heating the clusters to 800 K.

The changes to the cluster deposits upon heating was investigated by scanning transmission electron microscopy (STEM). STEM images of the particles supported on HOPG before and after the TDS experiments are shown in Figure 5B and C, respectively. The dropcast clusters assembled as films over the HOPG surface and the average size of the initially dispersed clusters was ~1.2 nm (Figure S21A) which is consistent with previous reports.[11] Heating the clusters on HOPG resulted in sintering of the clusters which resulted in an increase in the size of the particles to a mean size of ~1.8 nm (Figure S21B) as observed in STEM. We remind the reader in this context, that the STEM images of $[Pt_{17}(CO)_{12}(PPh_3)_8]Cl_x$ deposited on γ-Al_2O_3 by Negishi et al. showed retention of roughly the same average size and ellipsoidal shape of their central noble metal cluster core before and after calcination to 500 °C. Less sintering on γ-Al_2O_3 may reflect stronger metal−support interactions.[26,27] However, higher

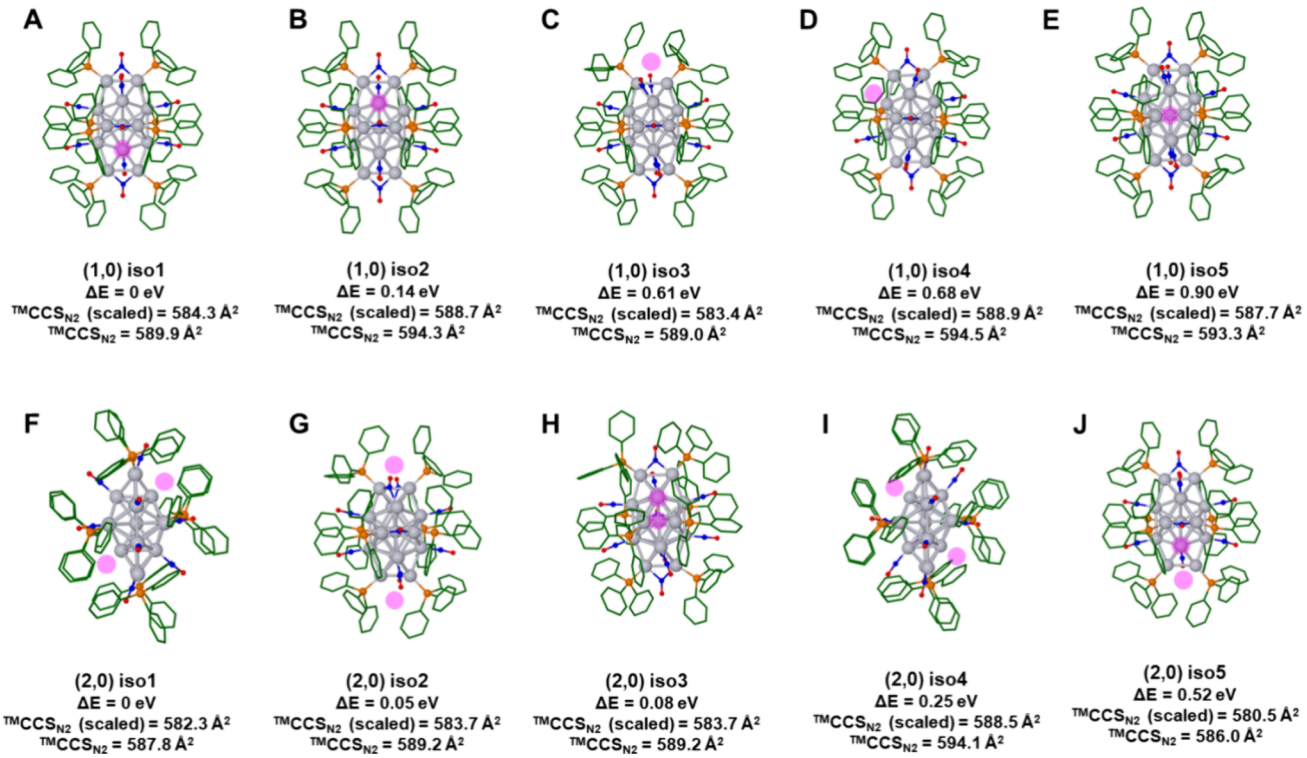

Figure 6. DFT-optimized candidate structures for (1,0) (A–E) and (2,0) (F–J) isomers together with their relative energies and calculated collision cross sections ($^{TM}CCS_{N2}$ (scaled) = 0.9906·$^{TM}CCS_{N2}$, scaling is by using precursor (0,0) ion as a reference to correct small errors between experimental and calculated CCS). Magenta colored circles mark sites where CO was removed. Color codes: gray: Pt atoms, orange: P atoms, blue and red: C and O of CO, green: C of C_6H_5 moieties of PPh_3 ligands, H atoms are not shown for clarity.

cluster loadings and different heating conditions were used in our TDS experiments.

3. MODELING AND DISCUSSION OF EXPERIMENTAL RESULTS

Heating $[Pt_{17}(CO)_{12}(PPh_3)_8](NO_3)_2$/HOPG leads to desorption of the same neutral molecules (CO, benzene and H_2) and in the same energetic ordering as for collisional excitation of isolated $[Pt_{17}(CO)_{12}(PPh_3)_8]^{2+}$. T his at first s ight s urprising observation implies that NO_3^- counterions, on-surface sintering processes and other types of cluster–cluster reactions which would be expected to change the desorption phenomenology relative to isolated clusters do not contribute strongly to the desorption signals.[28] As a corollary, the processes going on in gas-phase following collisional excitation of individual $[Pt_{17}(CO)_{12}(PPh_3)_8]^{2+}$ must clearly also be relevant to thermal decomposition of at least the topmost layers of microcrystalline $[Pt_{17}(CO)_{12}(PPh_3)_8](NO_3)_2$ on HOPG.

We therefore next return to and now more explicitly formulate the identified g as-phase u nimolecular d issociation r eactions. W e have observed three different collisional excitation energy regimes: (a) low collision voltages lead only to loss of CO, reaction 1, (b) intermediate collision voltages are associated with essentially concurrent benzene and (further) CO loss, reaction 2 and (c) high collision voltages lead also to the evolution of H_2.

$$[Pt_{17}(CO)_{12}(PPh_3)_8]^{2+} \rightarrow\rightarrow [Pt_{17}(CO)_{12-x}P_8C_{144}H_{120})]^{2+} + xCO (x = 1 - 3) \quad (1)$$

$$[Pt_{17}(CO)_{12-x}P_8C_{144}H_{120})]^{2+} \rightarrow\rightarrow \rightarrow [Pt_{17}(CO)_{12-x-y}P_8C_{144-6z}H_{120-6z})]^{2+} + yCO + zC_6H_6 \quad (2)$$

Note that we have written the reaction equations with partial sum formulas rather than discrete numbers of PPh_x moieties to emphasize the initially unknown structural evolution along the fragmentation cascade.

3.1. Isomeric Structures of (1,0) and (2,0). To characterize the CO desorption pathway, we calculated possible isomeric structures for (1,0) and (2,0) by removing one or two CO ligands from the (0,0) precursor structure followed by full geometry optimization at the DFT level of theory (see Methods). Corresponding theoretical collision cross sections were then determined with the trajectory method ($^{TM}CCS_{N2}$) as implemented in IMoS 1.09. Using the DFT-optimized structure of the parent dication (0,0) (structure in Figure 1A) which is based on the known crystal structure, we obtained $^{TM}CCS_{N2}$ of 593.3 Å^2, in good agreement with $^{TW}CCS_{N2}$ of 587.7 Å^2 (from high resolution 10 pass cIMS study). As small errors arise due to systematic limitations of both theory and experiment, to assign structures for isomers of *(m,0)* (*m* = 1–2) fragments which shows marginal CCS differences (Figure 4A-C) we use a scaling factor by using the precursor ion with its known structure as reference and adjusting its $^{TM}CCS_{N2}$ value from IMoS with a scaling factor to perfectly match the experimental $^{TW}CCS_{N2}$. The scaling factor is 587.7/593.3 = 0.9906 which we also apply to $^{TM}CCS_{N2}$ values determined for (1,0) and (2,0) fragment ions. Hence, we obtain a scaled $^{TM}CCS_{N2}$ of 587.7 Å^2 for (0,0). The precursor (0,0) shows several different types of μ_1 ("on-top") and μ_2 ("bridging") CO binding depending upon local symmetry and chemical environment. CO desorption could in principle occur from any of these nonequivalent sites (indicated in Figure S22). We therefore considered 5 such isomeric candidate structures for (1,0) species, as shown in Figure 6A-E. Among the calculated structures, (1,0) iso1, corresponding to loss of a μ_1-CO, was the lowest energy isomer and has $^{TM}CCS_{N2}$ (scaled) of 584.3 Å^2. The structure (1,0) iso3 with loss of a μ_2-CO from the apex position, showed $^{TM}CCS_{N2}$ (scaled) of 583.4 Å^2. The other isomeric structures i.e. (1,0) iso2, iso4 and iso5 showed larger $^{TM}CCS_{N2}$ (scaled) in the range 587.7 to 588.9 Å^2. Comparison of $^{TM}CCS_{N2}$ (scaled) to that of $^{TW}CCS_{N2}$ values suggests that (1,0) iso1,3 contributes to the smaller isomer ii ($^{TW}CCS_{N2}$ of

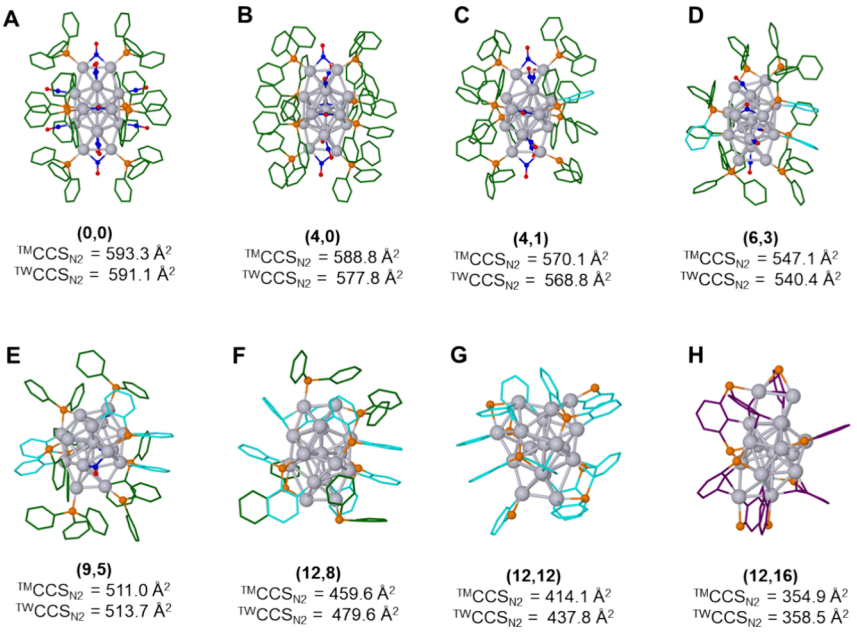

Figure 7. DFT optimized structures of parent cluster (A) (0,0) and selected *(m,n)* fragment ions, (B) (4,0), (C) (4,1), D) (6,3), (E) (9,5), (F) (12,8), (G) (12,12), and (H) (12,16). Color codes: gray: Pt, orange: P, blue and red: C and O of CO, green: C of C_6H_5 moieties, cyan: C of C_6H_4 moieties, purple: C of C_6H_3 moieties. H atoms are not shown for clarity. $^{TM}CCS_{N2}$ values are not scaled. $^{TW}CCS_{N2}$ values shown here are determined from single pass cIMS study.

583.0 Å^2) and (1,0) iso2,4,5 contribute to the larger isomer i ($^{TW}CCS_{N2}$ of 585.6 Å^2). The standard error in the values of $^{TM}CCS_{N2}$ for calculated structures of (1,0) isomers are in the range of ±0.4 Å^2 (see details in Table S2) and hence the structures of the two different isomers can clearly be distinguished and assigned through comparison between experiment and theory.

For fragment (2,0) we only calculated a few plausible structures due to the large number of possible isomers. The structures are shown in Figure 6F-J. We found three isomers for (2,0) (iso1, iso2 and iso3) within an energy window of 0.08 eV exhibiting $^{TM}CCS_{N2}$ (scaled) of 582.3, 583.7 and 583.7 Å^2, respectively. The structure (2,0) iso4 has slightly larger $^{TM}CCS_{N2}$ (scaled) of 588.5 Å^2 and (2,0) iso5 shows the smallest $^{TM}CCS_{N2}$ (scaled) of 580.5 Å^2. The structures (2,0) iso1,5 can be assigned to the experimentally observed isomer (ii) with $^{TW}CCS_{N2}$ of 580.1 Å^2. The other calculated isomer (2,0) structures, i.e. iso2–4, contribute to the broad range of isomers with an average $^{TW}CCS_{N2}$ of 585.5 Å^2 (i) observed in experiment. Among the structures studied, we did not find agreement for the smallest experimentally observed isomer of (2,0) with $^{TW}CCS_{N2}$ of 574.9 Å^2. However, as mentioned above, a greater number of isomeric structures of (2,0) are possible and a 2-fold CO vacancy isomer better describing the experiment may have been missed. Also, structures with C–H activation or with stronger interaction between C_6H_5 units (but no corresponding further fragmentation loss) are already possible. These could be studied in greater detail in future.

3.2. Structural Changes During the Full Cascade of Both CO and Benzene Desorptions. Structural models for the intermediate voltage regime, i.e. (*m,n*) fragments with $m > 2$ and $n > 0$ were first generated using GFN1-xTB[29] - a semiempirical extended tight binding method which is comparatively inexpensive computationally (versus DFT). xTB has recently been applied to Pt nanoparticles in the size range between Pt_{13} – Pt_{561} and for Pt carbonyl clusters.[30,31] The structural agreement (based on RMSD values) between the DFT structure of the intact $[Pt_{17}(CO)_{12}(PPh_3)_8]^{2+}$ cluster, (0,0), with GFN1-xTB was found to be better compared to GFN2-xTB[32] as shown in Figure S23. For this reason, we used the GFN1-xTB method for all semiempirical calculations and we fixed the positions of the Pt atoms and only relaxed the ligand layer as required (see details in SI).

Two different GFN1-xTB based approaches were used to generate structural models to compare with experiment. First, (*m,n*) fragment structures were generated by simply removing *m* CO units and *n* phenyl rings (C_6H_5) plus *n* additional H atoms (from neighboring phenyl rings of $[Pt_{17}(CO)_{12}(PPh_3)_8]^{2+}$) (Figure S24). For the resulting defect/vacancy structures, we then conducted single point calculations with GFN1-xTB to determine their $^{TM}CCS_{N2}$. Note that we have recently been able to describe fragment structures of alkynyl stabilized gold clusters with a similar approach.[13] In a second, more sophisticated approach which is described in more detail in SI and Figure S25, we were inspired by Koessler et al., who studied $[AuPt,(PPh_3)_3]^+$ ions in the gas-phase via CID and found that upon excitation these complexes lose benzene.[33] The authors performed DFT calculations to calculate the corresponding transition states and found C–H bond activation (of the ortho-H atoms in the phenyl rings) to be responsible for the loss of benzene. This occurs as the last step in a multistep reaction also involving H-transfer, phenyl group exchange and Pt–C bond formation.[33] The structures calculated by us (still using xTB) with the second approach accounting for CO loss, benzene loss and the successive formation of Pt–C bonds at each fragmentation step are shown in Figure S26 together with their $^{TM}CCS_{N2}$ values. Comparison of the $^{TM}CCS_{N2}$ obtained by the above two methods with $^{TW}CCS_{N2}$ values is presented in Figure S27. The better agreement suggests that the second more sophisticated approach involving relaxation of the ligand shell, accompanied by benzene loss and Pt–C bond formation provides a much better description of the experimental fragment structures.

A selection of well-fitting xTB derived fragment structures (second approach) was then subjected to a full DFT-based geometry optimization (now also including the Pt atoms). The structures resulting for (0,0), (4,0), (4,1), (6,3), (9,5), (12,8), (12,12) and (12,16) are shown in Figure 7 together with their $^{TM}CCS_{N2}$ values and compared to their respective $^{TW}CCS_{N2}$. First, the Pt_{17} core does not appear to rearrange significantly for fragments (4,0) (Figure 7B), (4,1) (Figure 7C) and (6,3) (Figure 7D) showing RMSD values of 0.17, 0.28 and 0.29 Å, respectively, with respect to the Pt_{17} core of precursor (0,0) (Figure S28). Progressive loss of benzene and concomitant Pt–C bond formation then begins to induce changes in the Pt framework leading to somewhat more spherical metal cores and increasingly more compact overall cluster topologies (Figure S28). In structure (12,8) (Figure 7F) all of the eight PPh_3 units have lost one phenyl ring (after H-transfer as benzenes) and eight Pt–C bonds have

been formed to Pt atoms that were previously bound to μ_1−CO units. As a consequence, each of the four lateral $P(C_6H_4)_2$ units are bound to at least two Pt atoms via direct or bridging Pt−C bonds. For comparison Figure S29 also shows an alternative structure in which eight $P(C_6H_5)(C_6H_4)$ units are present, each binding to at least one Pt atom with their C_6H_4 moieties.

Starting from (12,12), where all surface Pt (which were formerly bound to CO) become saturated (or "poisoned") by Pt−C bonds, further removal of C_6H_6 can involve the formation of C_6H_3 moieties each attached to the cluster core *via two Pt−C bonds* (in ortho and meta position to the P atom). This change in bonding configuration is likely responsible for the increased slope in $^{TW}CCS_{N2}$ versus mass loss that sets in at ∼ (12,10) in Figure 4E (the C_6 rings move significantly closer to the Pt_{17} core). A possible structure of (12,16), optimized by DFT is shown in Figure 7H. The comparison of $^{TM}CCS_{N2}$ to $^{TW}CCS_{N2}$ for the selected DFT-optimized fragments showed reasonable agreement (see Figure S30 and Table S1) thus enabling us to identify the onset of enhanced Pt−C bond formation as a plausible new pathway for further fragmentation. Please note that we did not make strict assignments for the smaller fragment structures, as this is not possible due to the large number of possible isomers. Instead, we illustrate that the general size dependency of the CCS values between experiment and theory is largely consistent.

4. CONCLUSIONS

Our gas phase studies show that increasing collisional excitation of $[Pt_{17}(CO)_{12}(PPh_3)_8]^{2+}$ first causes loss of 3−5 CO molecules freeing up a corresponding number of Pt sites. Further excitation also leads to benzene loss. This is likely involves activation of a C−H bond associated with one of the PPh_3 ligands (most likely catalyzed by Pt sites freed up by the initial CO desorption), Pt−C bond formation, transfer of the released H atom to another P-bound phenyl group and benzene release. As the excitation energy is raised further, benzene loss continues until all CO's are removed and all uncovered Pt sites are correspondingly functionalized (poisoned) by carbon. Interestingly, the Pt_{17} core (decorated with 8 P atoms) seems to be robustly retained over more than 24 fragmentation steps (of CO and benzene loss) − as indicated both by IMS measurements and calculations.

We observe qualitatively the same T-dependent desorption behavior for $[Pt_{17}(CO)_{12}(PPh_3)_8](NO_3)_2$ when deposited onto HOPG: only CO, benzene and H_2 are evolved upon heating. CO and benzene desorption signals show roughly the same T-dependence. Consistent with the CID measurements, the threshold desorption temperature for CO was marginally lower than that of benzene. Higher surface temperatures lead to more CO and benzene loss. Heating even further leads to H_2 evolution again in common with gas-phase (when CO and benzene desorption decreases).

For sufficient signal, all TDS measurements (of $[Pt_{17}(CO)_{12}(PPh_3)_8](NO_3)_2$ /HOPG) reported here had to be carried out on multilayer films. As already pointed out, TDS is expected to be particularly sensitive to decomposition in the topmost layers of this material. In particular, diffusion of any benzene formed further down in the film to its surface becomes increasingly unlikely the longer the diffusion path is. Instead, cation/counteranion reactions and/or interlinking of clusters (e.g., via C−H activation of the phenyl groups of adjacent clusters) should become relatively more important in the more coordinated subsurface environment. As a result, an inhomogeneous material consisting of $Pt_{17}P_8$-derived sintered particles embedded in an amorphous carbon matrix can be envisaged to form upon heating to 800 K as supported by our STEM images

To sort out active sites for oxidation catalysis (see introduction), it would clearly also be interesting to study the activation of supported clusters in a reactant atmosphere. Further experiments along these lines will be explored in future.

5. METHODS

5.1. Cluster Preparation. $[Pt_{17}(CO)_{12}(PPh_3)_8](NO_3)_2$ clusters were synthesized and purified following a reported procedure with slight modifications.[9,11] A more detailed synthetic method description is presented in the Supporting Information. Moreover, using the same synthetic procedure, we synthesized an isotopically labeled cluster with deuterated PPh_3 (PPh_3-d15).

5.2. Thermal Desorption Spectroscopy (TDS; Depo-0). $[Pt_{17}(CO)_{12}(PPh_3)_8](NO_3)_2$ solutions (in 1:1 methanol/toluene) of known concentration were drop cast onto ∼1 cm^2 HOPG supports, dried under ambient conditions and then inserted into a custom P- and T- variable, UHV compatible reactor, Depo-0, for *m*/*z*-resolved TDS. Measurements were typically performed on ca. 0.5 mg of deposited material (see SI for further details on sample preparation for TDS). Depo-0 comprises: (i) a differentially pumped quadrupole mass spectrometer (QMS) equipped with an electron impact ion source and with a nominal mass resolution below 0.5 *m*/*z* and (ii) a reaction chamber with a base pressure $<5 \times 10^{-9}$ mbar in which samples can be heated from 250−1000 K. The sample temperature was determined using a thermocouple sensor inserted into the sample holder and is subject to an error of ca. ± 20 K (relative desorption temperatures determined for different species during the same heating ramp are more accurate). Figure S31 shows a schematic of the Depo-0 setup. For this, samples held ca. 1 mm from the entrance to the QMS chamber were first evacuated to below 10^{-8} mbar and then heated from room temperature at typical heating rates of 1.0−1.2 K s^{-1} while iteratively recording the ion signal at different preset *m*/*z* values.

5.3. High Resolution Electrospray Ionization Mass Spectrometry (ESI MS), Collision Induced Dissociation (CID), and Ion Mobility Spectrometry (IMS). ESI MS, CID and IMS measurements were performed using a commercially available instrument, Waters Select Series Cyclic IMS[12] with an electrospray source. This instrument enabled us to measure (i) mass spectra, (ii) CID spectra of *m*/*z*-selected ions and (iii) traveling wave (TW) IMS separation in N_2 buffer gas to determine ion mobilities and the corresponding experimental collision cross sections ($^{TW}CCS_{N2}$). The instrument has been extensively described elsewhere.[12] Note that the wide natural isotopologue distribution corresponding to 17 Pt atoms requires high mass resolution to properly analyze the fragment distributions (the Cyclic IMS-MS has sufficient nominal mass resolution >100,000 (fwhm)).

Electrospray conditions were as follows: ca. 1 mM solution of $[Pt_{17}(CO)_{12}(PPh_3)_8](NO_3)_2$ in a 1:1 mixture of toluene and methanol solvent, capillary voltage: 3 kV; source temperature: 100 °C, desolvation temperature: 200 °C, desolvation gas flow: 800 L/h. For CID measurements, the ions of interest were first *m*/*z*-selected using the quadrupole mass filter and fragmentation was performed in the "trap" chamber by increasing the collision voltage in the range of 2−120 V. For performing IMS studies, ions are injected into a roughly circular 1 m traveling wave drift cell filled with N_2 and analyzed by pulsing them out into a dual reflectron time-of-flight mass spectrometer after a set number of measurement cycles. The higher the number of passes/cycles the better the CCS resolution until the ion packet of interest begins to catch up with itself. Resolutions (CCS/ΔCCS) of greater than 700 have been reported for single isomer/conformer ions cycled 100 times.[12] To determine the mobilities of the fragmented ions, CID experiments of the parent ion at varied collision voltages (2−120 V) was first performed in the "trap" chamber to observe the desired fragments. The resulting fragment ions were then injected into the cyclic IMS drift cell where they were subsequently separated. Note that only a certain range of fragments can be formed at a particular collision voltage, so the applied collision voltages were varied to obtain the arrival time

distributions of the complete series of fragments as discussed. The following traveling wave (TW) parameters were used for the IMS measurements: cyclic TW velocity: 375 m/s, array TW velocity: 375 m/s, TW static height: 18 V, TW ramp start height: 15 V, TW ramp end height: 35 V, TW ramping rate: 2.5 V/ms. Cyclic IMS (cIMS) procedures followed in this study (regarding calibration using Agilent tuning mix, calculation of $^{TW}CCS_{N2}$ from recorded arrival times, etc.) correspond closely to those used by us in a recent study of transition metal doped, ligand stabilized gold clusters.[13] For single pass measurement, the data was processed by determining the drift times from Gaussian fits of the extracted arrival time distributions (corresponding to specific masses of the fragment) which was subsequently converted to $^{TW}CCS_{N2}$ following the calibration method. Details on the calibration procedure is provided in the Supporting Information and calibration curves are presented in Figure S32.

5.4. Scanning Transmission Electron Microscopy (STEM). STEM measurements were performed using a Themis Z transmission electron microscope (TEM) (Thermofisher Scientific), operated at 300 kV. The particles supported on HOPG were transferred to amorphous carbon-coated holey Cu grids for the TEM analysis by scraping out the top layers of HOPG directly with the TEM grid. Note that a relatively high concentration of clusters (0.5 mg over 1 cm^2 HOPG) was used, so the clusters were assembled as films (and not isolated) as observed in STEM. For particle size analysis, around 200 particles in each case was analyzed from different areas of the HOPG surface.

5.5. Computational Methods. *5.5.1. DFT Calculations.* Structures of the precursor ion $[Pt_{17}(CO)_{12}(PPh_3)_8]^{2+}$ and its fragments were initially calculated with the semiempirical extended tight binding method GFN1-xTB[39,34] and some structures were refined with DFT in TURBOMOLE 7.4[35] using the PBE functional[36] with def2-SVP basis sets[37] and accounting for dispersion interactions at the DFT-D3 bj level.[38,39] The crystal structure of $[Pt_{17}(CO)_{12}(PPh_3)_8]^{2+}$ (without the counteranions) was used as starting structure.[9] To prevent SCF (self-consistent-field) convergence problems we used Fermi smearing as implemented in TURBOMOLE.

5.5.2. Trajectory Calculations. The calculation of $^{TM}CCS_{N2}$ were performed with IMoS 1.09 using the trajectory method (TM) in N_2 gas.[40] Atomic coordinates and NBO partial charges obtained from the DFT calculations were used as the input for the trajectory calculations to obtain $^{TM}CCS_{N2}$. The trajectory calculations were carried out at 300 K and the ion-induced quadrupole potential was not considered for the trajectory simulations.

For the precursor ion and close-lying larger fragments, i.e., when only CO is lost, we simulated 3×10^7 trajectories to reduce the statistical error, for all other smaller fragments (including also benzene loss) we used 3×10^6 trajectories. For 3×10^7 trajectories the statistical error in $^{TM}CCS_{N2}$ is around ±0.06% and for 3×10^6 trajectories it is around ±0.17%. Details on statistical error calculation for the trajectory methods is discussed in the Supporting Information (Table S2).

AUTHOR INFORMATION

Corresponding Author

Manfred M. Kappes − *Institute of Physical Chemistry, Karlsruhe Institute of Technology, Karlsruhe 76131, Germany; Institute of Nanotechnology, Karlsruhe Institute of Technology, Karlsruhe 76131, Germany;* orcid.org/0000-0002-1199-1730; Email: manfred.kappes@kit.edu

Authors

Papri Chakraborty − *Institute of Physical Chemistry, Karlsruhe Institute of Technology, Karlsruhe 76131, Germany; Institute of Nanotechnology, Karlsruhe Institute of Technology, Karlsruhe 76131, Germany;* orcid.org/0000-0002-1353-7734

Marco Neumaier − *Institute of Nanotechnology, Karlsruhe Institute of Technology, Karlsruhe 76131, Germany;* orcid.org/0000-0002-3810-3377

Johannes Seibel − *Institute of Physical Chemistry, Karlsruhe Institute of Technology, Karlsruhe 76131, Germany*

Nicola Da Roit − *Institute of Catalysis Research and Technology, Karlsruhe Institute of Technology, Karlsruhe 76131, Germany*

Artur Böttcher − *Institute of Physical Chemistry, Karlsruhe Institute of Technology, Karlsruhe 76131, Germany;* orcid.org/0000-0001-8477-1336

Christian Schmitt − *Institute of Catalysis Research and Technology, Karlsruhe Institute of Technology, Karlsruhe 76131, Germany*

Di Wang − *Institute of Nanotechnology, Karlsruhe Institute of Technology, Karlsruhe 76131, Germany;* orcid.org/0000-0001-9817-7047

Christian Kübel − *Institute of Nanotechnology, Karlsruhe Institute of Technology, Karlsruhe 76131, Germany;* orcid.org/0000-0001-5701-4006

Silke Behrens − *Institute of Catalysis Research and Technology, Karlsruhe Institute of Technology, Karlsruhe 76131, Germany;* orcid.org/0000-0003-4328-9564

Author Contributions

P.C. and M.N. contributed equally to this work.

Author Contributions

P.C. and M.N. performed the ESI MS and CID measurements. P.C. carried out the ion mobility experiments and analysis. J.S. and P.C. performed the thermal desorption studies. M.N. performed the computations. A.B. designed the Depo-0 instrument. N.D.R. and C.S. performed the cluster synthesis under the supervision of S.B. STEM measurements were performed by D.W. under the supervision of C.K. The manuscript was written by P.C., M.N., and M.M.K. with contributions of all authors including their comments on interpretation of the results. The project was supervised by M.M.K.

Notes

The authors declare no competing financial interest.

ACKNOWLEDGMENTS

MK, CK and SB thank the German Science Foundation (DFG) for generous support of this research under projects A02, B01 and B02 of the collaborative research center "TrackAct" (CRC 1441). MK also gratefully acknowledges

funding of a Waters Select Series Cyclic IMS by KIT and DFG (under Art. 91b GG). The authors acknowledge the Karlsruhe Nano Micro Facility (KNMFi) for ST EM measurements. Authors thank Dr. Patrick Weis for his suggestions and discussions on the cyclic ion mobility data analysis.

REFERENCES

(1) Heck, R. M.; Farrauto, R. J.; Gulati, S. T. *Catalytic Air Pollution Control: Commercial Technology*. 3rd ed.; John WILEY & Sons: 2009.
(2) Agote-Arán, M.; Elsener, M.; Schütze, F. W.; Schilling, C. M.; Sridhar, M.; Katsaounis, E.; Kröcher, O.; Ferri, D. Understanding the Impact of Poison Distribution on the Performance of Diesel Oxidation Catalysts. *Appl. Catal. B: Environmental* **2021**, *299*, No. 120684.
(3) Wang, X.; Zhao, J.; Eliasson, H.; Erni, R.; Ziarati, A.; McKeown Walker, S.; Bürgi, T. Very Low Temperature CO Oxidation over Atomically Precise Au_{25} Nanoclusters on MnO_2. *J. Am. Chem. Soc.* **2023**, *145*, 27273−27281.
(4) Sakamoto, K.; Masuda, S.; Takano, S.; Tsukuda, T. Partially Thiolated Au_{25} Cluster Anchored on Carbon Support Via Noncovalent Ligand−Support Interactions: Active and Robust Catalyst for Aerobic Oxidation of Alcohols. *ACS Catal.* **2023**, *13*, 3263−3271.
(5) Yamazoe, S.; Yoskamtorn, T.; Takano, S.; Yadnum, S.; Limtrakul, J.; Tsukuda, T. Controlled Synthesis of Carbon-Supported Gold Clusters for Rational Catalyst Design. *Chem. Rec.* **2016**, *16*, 2338−2348.
(6) Truttmann, V.; Drexler, H.; Stöger-Pollach, M.; Kawawaki, T.; Negishi, Y.; Barrabés, N.; Rupprechter, G. CeO_2 Supported Gold Nanocluster Catalysts for CO Oxidation: Surface Evolution Influenced by the Ligand Shell. *ChemCatChem.* **2022**, *14*, No. e202200322.
(7) Pollitt, S.; Truttmann, V.; Haunold, T.; Garcia, C.; Olszewski, W.; Llorca, J.; Barrabés, N.; Rupprechter, G. The Dynamic Structure of $Au_{38}(SR)_{24}$ Nanoclusters Supported on CeO_2 Upon Pretreatment and CO Oxidation. *ACS Catal.* **2020**, *10*, 6144−6148.
(8) Sulaiman, K. O.; Sudheeshkumar, V.; Scott, R. W. J. Activation of Atomically Precise Silver Clusters on Carbon Supports for Styrene Oxidation Reactions. *RSC Adv.* **2019**, *9*, 28019−28027.
(9) Nair, L. V.; Hossain, S.; Wakayama, S.; Takagi, S.; Yoshioka, M.; Maekawa, J.; Harasawa, A.; Kumar, B.; Niihori, Y.; Kurashige, W.; Negishi, Y. $[Pt_{17}(CO)_{12}(PPh_3)_8]^{n+}$ (n = 1, 2): Synthesis and Geometric and Electronic Structures. *J. Phys. Chem. C* **2017**, *121*, 11002−11009.
(10) Negishi, Y.; Shimizu, N.; Funai, K.; Kaneko, R.; Wakamatsu, K.; Harasawa, A.; Hossain, S.; Schuster, M. E.; Ozkaya, D.; Kurashige, W.; Kawawaki, T.; Yamazoe, S.; Nagaoka, S. γ-Alumina-Supported Pt_{17} Cluster: Controlled Loading, Geometrical Structure, and Size-Specific Catalytic Activity for Carbon Monoxide and Propylene Oxidation. *Nanoscale Adv.* **2020**, *2*, 669−678.
(11) Schmitt, C.; Da Roit, N.; Neumaier, M.; Maliakkal, C. B.; Wang, D.; Henrich, T.; Kübel, C.; Kappes, M.; Behrens, S. Continuous Flow Synthesis of Atom-Precise Platinum Clusters. *Nanoscale Adv.* **2024**, *6*, 2459−2468.
(12) Giles, K.; Ujma, J.; Wildgoose, J.; Pringle, S.; Richardson, K.; Langridge, D.; Green, M. A Cyclic Ion Mobility-Mass Spectrometry System. *Anal. Chem.* **2019**, *91*, 8564−8573.
(13) Hennrich, F.; Ito, S.; Weis, P.; Neumaier, M.; Takano, S.; Tsukuda, T.; Kappes, M. M. Cyclic Ion Mobility of Doped $[MAu_{24}L_{18}]^{2-}$ Superatoms and Their Fragments (M = Ni, Pd and Pt; L = Alkynyl). *Phys. Chem. Chem. Phys.* **2024**, *26*, 8408−8418.
(14) Chakraborty, P.; Malola, S.; Neumaier, M.; Weis, P.; Häkkinen, H.; Kappes, M. M. Elucidating the Structures of Intermediate Fragments During Stepwise Dissociation of Monolayer-Protected Silver Clusters. *Angew. Chem., Int. Ed.* **2023**, *62*, No. e202305836.
(15) Chakraborty, P.; Malola, S.; Weis, P.; Neumaier, M.; Schneider, E. K.; Häkkinen, H.; Kappes, M. M. Tailoring Vacancy Defects in Isolated Atomically Precise Silver Clusters through Mercury-Doped Intermediates. *J. Phys. Chem. Lett.* **2023**, *14*, 11659−11664.
(16) Neumaier, M.; Baksi, A.; Weis, P.; Schneider, E. K.; Chakraborty, P.; Hahn, H.; Pradeep, T.; Kappes, M. M. Kinetics of Intercluster Reactions between Atomically Precise Noble Metal Clusters $[Ag_{25}(DMBT)_{18}]^-$ and $[Au_{25}(PET)_{18}]^-$ in Room Temperature Solutions. *J. Am. Chem. Soc.* **2021**, *143*, 6969−6980.
(17) Johnson, G. E.; Priest, T.; Laskin, J. Size-Dependent Stability toward Dissociation and Ligand Binding Energies of Phosphine Ligated Gold Cluster Ions. *Chem. Sci.* **2014**, *5*, 3275−3286.
(18) Ghosh, A.; Bodiuzzaman, M.; Nag, A.; Jash, M.; Baksi, A.; Pradeep, T. Sequential Dihydrogen Desorption from Hydride-Protected Atomically Precise Silver Clusters and the Formation of Naked Clusters in the Gas Phase. *ACS Nano* **2017**, *11*, 11145−11151.
(19) Gao, W.; Zheng, W. T.; Jiang, Q. Dehydrogenation of Benzene on Pt(111) Surface. *J. Chem. Phys.* **2008**, *129*, No. 164705.
(20) Saeys, M.; Reyniers, M.-F.; Neurock, M.; Marin, G. B. Density Functional Theory Analysis of Benzene (De)Hydrogenation on Pt(111): Addition and Removal of the First Two H-Atoms. *J. Phys. Chem. B* **2003**, *107*, 3844−3855.
(21) Angel, L. A.; Majors, L. T.; Dharmaratne, A. C.; Dass, A. Ion Mobility Mass Spectrometry of $Au_{25}(SCH_2CH_2Ph)_{18}$ Nanoclusters. *ACS Nano* **2010**, *4*, 4691−4700.
(22) Daly, S.; Choi, C. M.; Zavras, A.; Krstić, M.; Chirot, F.; Connell, T. U.; Williams, S. J.; Donnelly, P. S.; Antoine, R.; Giuliani, A.; Bonačić-Koutecký, V.; Dugourd, P.; O'Hair, R. A. J. Gas-Phase Structural and Optical Properties of Homo- and Heterobimetallic Rhombic Dodecahedral Nanoclusters $[Ag_{14-n}Cu_n(C{\equiv}C^tBu)_{12}X]^+$ (X = Cl and Br): Ion Mobility, VUV and UV Spectroscopy, and DFT Calculations. *J. Phys. Chem. C* **2017**, *121*, 10719−10727.
(23) Geue, N.; Winpenny, R. E. P.; Barran, P. E. Ion Mobility Mass Spectrometry for Large Synthetic Molecules: Expanding the Analytical Toolbox. *J. Am. Chem. Soc.* **2024**, *146*, 8800−8819.
(24) Geue, N.; Bennett, T. S.; Arama, A.-A.-M.; Ramakers, L. A. I.; Whitehead, G. F. S.; Timco, G. A.; Armentrout, P. B.; McInnes, E. J. L.; Burton, N. A.; Winpenny, R. E. P.; Barran, P. E. Disassembly Mechanisms and Energetics of Polymetallic Rings and Rotaxanes. *J. Am. Chem. Soc.* **2022**, *144*, 22528−22539.
(25) Su, P.; Zhu, X.; Wilson, S. M.; Feng, Y.; Samayoa-Oviedo, H. Y.; Sonnendecker, C.; Smith, A. J.; Zimmermann, W.; Laskin, J. The Effect of Host Size on Binding in Host−Guest Complexes of Cyclodextrins and Polyoxometalates. *Chem. Sci.* **2024**, *15*, 11825−11836.
(26) Poths, P.; Hong, Z.; Li, G.; Anderson, S. L.; Alexandrova, A. N. "Magic" Sinter-Resistant Cluster Sizes of Pt_n Supported on Alumina. *J. Phys. Chem. Lett.* **2022**, *13*, 11044−11050.
(27) Kaiser, S.; Plansky, J.; Krinninger, M.; Shavorskiy, A.; Zhu, S.; Heiz, U.; Esch, F.; Lechner, B. A. J. Does Cluster Encapsulation Inhibit Sintering? Stabilization of Size-Selected Pt Clusters on $Fe_3O_4(001)$ by SMSI. *ACS Catal.* **2023**, *13*, 6203−6213.
(28) Weippert, J.; Huber, P.; Hauns, J.; Narita, A.; Müllen, K.; Amsharov, K. Y.; Böttcher, A.; Kappes, M. M. Comparative Study of Direct and Graphite-Mediated Oxidation of Large PAHs. *J. Phys. Chem. C* **2021**, *125*, 8163−8176.
(29) Bannwarth, C.; Caldeweyher, E.; Ehlert, S.; Hansen, A.; Pracht, P.; Seibert, J.; Spicher, S.; Grimme, S. Extended Tight-Binding Quantum Chemistry Methods. *WIREs Comput. Mol. Sci.* **2021**, *11*, No. e1493.
(30) Cesari, C.; Berti, B.; Funaioli, T.; Femoni, C.; Iapalucci, M. C.; Pontiroli, D.; Magnani, G.; Riccò, M.; Bortoluzzi, M.; Vivaldi, F. M.; Zacchini, S. Atomically Precise Platinum Carbonyl Nanoclusters: Synthesis, Total Structure, and Electrochemical Investigation of $[Pt_{27}(CO)_{31}]^{4-}$ Displaying a Defective Structure. *Inorg. Chem.* **2022**, *61*, 12534−12544.
(31) Ricchebuono, A.; Vottero, E.; Piovano, A.; Groppo, E.; Raybaud, P.; Chizallet, C. Assessing Low-Cost Computational Methods against Structural Properties and Size Effects of Pt Nanoparticles. *J. Phys. Chem. C* **2023**, *127*, 18454−18465.
(32) Bannwarth, C.; Ehlert, S.; Grimme, S. GFN2-xTB-an Accurate and Broadly Parametrized Self-Consistent Tight-Binding Quantum Chemical Method with Multipole Electrostatics and Density-Depend-

ent Dispersion Contributions. *J. Chem. Theory Comput.* **2019**, *15*, 1652−1671.
(33) Koessler, K.; Scherer, H.; Butschke, B. Phenyl-Group Exchange in Triphenylphosphine Mediated by Cationic Gold−Platinum Complexes—a Gas-Phase Mimetic Approach. *Inorg. Chem.* **2020**, *59*, 9496−9510.
(34) Grimme, S.; Bannwarth, C.; Shushkov, P. A Robust and Accurate Tight-Binding Quantum Chemical Method for Structures, Vibrational Frequencies, and Noncovalent Interactions of Large Molecular Systems Parametrized for All spd-Block Elements (Z = 1−86). *J. Chem. Theory Comput.* **2017**, *13*, 1989−2009.
(35) Ahlrichs, R.; Bär, M.; Häser, M.; Horn, H.; Kölmel, C. Electronic Structure Calculations on Workstation Computers: The Program System Turbomole. *Chem. Phys. Lett.* **1989**, *162*, 165−169.
(36) Perdew, J. P.; Burke, K.; Ernzerhof, M. Generalized Gradient Approximation Made Simple. *Phys. Rev. Lett.* **1996**, *77*, 3865−3868.
(37) Weigend, F.; Ahlrichs, R. Balanced Basis Sets of Split Valence, Triple Zeta Valence and Quadruple Zeta Valence Quality for H to Rn: Design and Assessment of Accuracy. *Phys. Chem. Chem. Phys.* **2005**, *7*, 3297−3305.
(38) Grimme, S.; Antony, J.; Ehrlich, S.; Krieg, H. A Consistent and Accurate Ab Initio Parametrization of Density Functional Dispersion Correction (DFT-D) for the 94 Elements H-Pu. *J. Chem. Phys.* **2010**, *132*, No. 154104.
(39) Grimme, S.; Ehrlich, S.; Goerigk, L. Effect of the Damping Function in Dispersion Corrected Density Functional Theory. *J. Comput. Chem.* **2011**, *32*, 1456−1465.
(40) Larriba-Andaluz, C.; Hogan, C. J., Jr. Collision Cross Section Calculations for Polyatomic Ions Considering Rotating Diatomic/Linear Gas Molecules. *J. Chem. Phys.* **2014**, *141*, No. 194107.